Rationalizing the structural changes and spectra of manganese and their temperature dependence in a series of garnets with first-principles calculations

Qiaoling Chen [1,2,3] Longbing Shang [1,2,3] Haoming Xu [1,2,3] Chonggeng Ma,[4] Peter A. Tanner [5,*] and Chang-Kui Duan [1,2,3,†]

[1]*Hefei National Laboratory for Physical Sciences at the Microscale and School of Physical Sciences, University of Science and Technology of China, Hefei 230026, China*

[2]*CAS Key Laboratory of Microscale Magnetic Resonance, University of Science and Technology of China, Hefei 230026, China*

[3]*CAS Center for Excellence in Quantum Information and Quantum Physics, University of Science and Technology of China, Hefei 230026, China*

[4]*School of Optoelectronic Engineering & CQUPT-BUL Innovation Institute, Chongqing University of Posts and Telecommunications, Chongqing 400065, China*

[5]*Hong Kong Baptist University, Department of Chemistry, Kowloon Tong, 224 Waterloo Rd, Hong Kong, China*

(Received 29 November 2021; accepted 24 January 2022; published 31 January 2022)

Detailed first-principles calculations have been carried out to study the stabilization, excitation and luminescence mechanisms of the ion Mn^{3+} in a series of $A_3B_2B'_3O_{12}$ garnet hosts. The formation energy shows that Mn^{3+} is dominant and is situated at the octahedral B site. The excited states, excitation, and emission energies of Mn^{3+} have then been calculated. The calculated energy levels of Mn^{3+} confirm that the red emission is due to the $^5T_2 \rightarrow {}^5E'$ transition and the near-infrared (NIR) emission arises from the $^1T_2 \rightarrow {}^3T_1$ transition. The populations of the $^5T_2$ and $^1T_2$ excited states and the corresponding radiative rates lead to the temperature dependence of the red to NIR emission. Furthermore, the adiabatic potential energy surfaces along the A_{1g} and E_g moeity modes of $[MnO_6]$ have been calculated and fitted well in the harmonic approximation. The high activation energy for Mn^{3+} indicates a low nonradiative multiphonon relaxation rate of $^5T_2$ to $^3T_1$. Hence, the ionization process was considered, and we show that it is responsible for the luminescence quenching of Mn^{3+}, so that the luminescence has rarely been reported experimentally. This work illustrates a well-designed approach based on the density-functional theory framework to predict the optical transition properties of the transition metal ion Mn^{3+} by calculating the structural distortions due to the Jahn-Teller effect, the optical transitions, quenching processes and the influence of pressure.

DOI: 10.1103/PhysRevB.105.035158

I. INTRODUCTION

The transition metal manganese is attractive for the nontrivial interplay of charge, spin, lattice and orbital freedom degrees, which are essential for the engineering of magnetism [1], multiferroic [2], photoluminescence [3], and many other properties [4]. The transition metal manganese can present multiple valence states, from Mn^{2+} to Mn^{7+} [5,6] and their distinct energy-level distributions give rise to different optical transition behaviors. For instance, the activator Mn^{4+} in general exhibits broad excitation bands in the ultraviolet-blue spectral region and sharp red emission lines in the visible spectral region [7,8]. By contrast, green to red and even near-infrared (NIR) emissions have been reported for Mn^{2+}, depending greatly on the ligand environment [9]. The ions Mn^{2+} and Mn^{4+} have been widely studied for their outstanding color rendering index and correlated color temperature as phosphor-converted white light-emitting diodes [10,11]. The intermediate valence state, Mn^{3+}, can be stable under the relevant chemical potential [12] and it is critically important for luminescence engineering [13,14]. However, the overlapped spectra of Mn^{3+} and Mn^{2+} enhance the difficulty of luminescence identification [15,16]. Thus a systematic study of the optical transition characteristics and an effective and predictive method for the luminescence of Mn^{3+} are urgently needed.

Besides, Mn^{3+} can trigger unique physical properties, such as the Jahn-Teller effect, magnetic properties, the temperature dependent red to NIR luminescence and the quenching of photoluminescence. For instance, the anti-Jahn-Teller polaron leads to the antiferromagnetic to ferromagnetic transition in $LaMnO_3$ [17]. The room-temperature ferromagnetism has been studied in Mn-doped $CH_3NH_3PbI_3$ perovskite and it originates from the double exchange interaction between Mn^{2+}–I^-–Mn^{3+} ions [18,19]. The Mn-Mn superexchange interactions lead to a blue shift of an on-site Mn^{3+} $d-d$ transition in multiferroic $RMnO_3$ [20,21] and the detailed study of the optical characteristics is important. The luminescence of the Mn^{3+} ion has previously been reported in garnet, kyanite, grossular, beryl and yttrium orthoaluminate crystals [22–25]. The temperature dependent luminescence has been studied in garnet crystals [23,24], whereas by contrast the emission

*peter.a.tanner@gmail.com.
†ckduan@ustc.edu.cn.

from Mn^{3+} is lacking in $YAlO_3$ [25]. Furthermore, it has been pointed out that Mn^{3+}, with a $3d^4$ electronic configuration, can exhibit a strong Jahn-Teller distortion in the ^5E ground state in octahedral coordination [24,26], which can strongly influence the optical spectra and luminescence quenching of transition-metal-ion-doped materials [27,28]. Up to now, the analysis and interpretation of the experimental results that have been attributed to Mn^{3+} are based on the phenomenological Tanabe-Sugano model. However, reliable first-principles calculations are lacking but are essential for identifying the experimental observations with more certainty and in revealing the detailed underlying mechanisms.

First-principles calculations have emerged as a predictive tool in the identification and characterization of the stabilization and luminescence [29] of activator centers, such as Ce^{3+} [30], Bi^{3+} [31] and Mn^{4+} [32]. Here in our present work, the Mn-activated garnets, $Y_3Al_5O_{12}$ (YAG), $Y_3Ga_5O_{12}$ (YGG), $Gd_3Ga_5O_{12}$ (GGG), and $Ca_3Ga_2Ge_3O_{12}$ (CGGG), have been chosen based on the fact that garnets are important solid-state laser host materials [33] and the experimental results are abundant for testing our calculations [23,24]. We have studied the site occupancy and valence states of manganese under relevant chemical conditions and reveal the Jahn-Teller effect on Mn^{3+}. Then, the excited states and the excitation and emission energies of dominant Mn^{3+} are deduced and presented. In particular, the temperature-dependent emissions in a series of garnets are discussed and attributed to the competition of $^5T_2 \rightarrow {}^5E'$ and $^1T_2 \rightarrow {}^3T_1$ transitions. Notably, the effects of ligand environment and pressure have been considered. The electron-phonon coupling on de-excitation phenomena through nonradiative multiphonon relaxation is analyzed by the adiabatic potential energy surface (APES), which is an important property for describing photochemical and photophysical processes in chemistry, biology, and materials science [34]. The nonradiative decay route, which is critically important for the luminescent engineering of Mn^{3+}, is analyzed by multiphonon relaxation and ionization processes.

II. METHODS

A. Parameter settings

All calculations have been performed in the framework of density-functional theory (DFT) implemented in the Vienna *ab initio* simulation package (VASP) code [35,36]. The interaction between ions and electrons is described by the projector augmented wave method [37] and the exchange correlation functional is given by the generalized gradient approximation (GGA) of the Perdew-Burke-Ernzerhof (PBE) functional [38]. The lattice parameters are relaxed using a 400 eV cutoff energy and a $3 \times 3 \times 3$ k-point mesh, deviate slightly from experimental results [39–42] by -0.4% to 0.1%, but would be overestimated by a larger cutoff energy. Thus we adopt the experimentally measured lattice parameters under ambient conditions (ICSD-41144, ICSD-185862, ICSD-192181, and ICSD-195450) for the calculations. Defect calculations are modeled with the periodic supercell formalism, and the conventional unit cell of garnet with 160 ions is used. The settings $U = 4$ eV and $J = 1$ eV, i.e., $U_{\text{eff}} = 3$ eV, are applied for the on-site Coulomb correction of transition metal manganese in the GGA+U scheme [43]. The defect geometric optimizations are calculated at the GGA+U level and the energies are calculated at the hybrid HSE06 level [44,45], unless otherwise stated. Geometric optimization is performed by the conjugate gradient technique until the scale of the Hellmann-Feynman forces on atoms is less than 0.01 eV/Å. As a compromise between accuracy and the computational resources of hybrid HSE06 calculations, 400 eV has been applied for the kinetic energy cutoff and only one Γ point is applied to sample the Brillouin zone. To confirm the reliability of our approach, we have performed the tests of the influence of different U_{eff}, k-point meshes and HSE06 on optimized structures and transition energies, which are discussed in detail in Note 1 of the Supplemental Material [46]. The results show that the deviation of transition energies obtained by different parameter settings is no more than 0.1 eV, not affecting our conclusion.

B. Formation energy of a point defect

The formation energy of a defect X in the charge state of q is defined as [29]

$$E^f[X^q] = E_{\text{tot}}[X^q] - E_{\text{tot}}[\text{bulk}] - \sum_i n_i\mu_i + qE_F, \quad (1)$$

where $E_{\text{tot}}[X^q]$ is the total energy derived from a supercell containing the defect, and $E_{\text{tot}}[\text{bulk}]$ is the total energy of the corresponding pristine supercell; n_i is the change in the number of type i atom species, which is added to ($n_i > 0$) and/or removed from ($n_i < 0$) the perfect supercell; μ_i is the relative chemical potential for type i atom species and E_F is the electron Fermi energy. *Post hoc* corrections to the total energy of charged defects are employed and we follow the method proposed by Durrant *et al.* [54], where the combination of the Lany-Zunger correction [55,56] due to image charge and the potential alignment between neutral systems was shown to yield accurate corrections for cubic supercells. More details are available in Note 2 of the Supplemental Material [46].

The defect concentration is related to the Gibbs energy of formation, which is usually approximated with the formation energy for solid phases [29,57]. Hence we have the following expression [57,58]:

$$c/N_{\text{sites}} = \omega \exp(-E^f/k_B T). \quad (2)$$

Here E^f is the formation energy calculated by Eq. (1), T is the temperature at which the defects reach thermal equilibrium distribution and is usually close to the temperature of synthesis or annealing, and N_{sites} and ω are the numbers of available atomic sites for doping and the degeneracy factor of the defect, respectively.

C. Excited state and geometric optimization

In the DFT framework, a spin multiplicity control method [59,60] supplemented by a constrained occupancy approach [30,61] is adopted for the excited-state calculations. In the presence of octahedral ligands, the five $3d$ orbitals split into the higher twofold degenerate e orbitals and the lower threefold degenerate t_2 orbitals. The ground state of Mn^{3+} is the Jahn-Teller-split $^5E'$ state with the $t_2^3e^1$ electronic

configuration, which can be obtained by spin quintet setting in the DFT framework. Then, the excited-states $|\,(t_2^2e^2)\,{}^5\mathrm{T}_2\rangle$, $|\,(t_2^4)\,{}^3\mathrm{T}_1\rangle$, $|\,(t_2^4)\,{}^1\mathrm{T}_2\rangle$ are considered. Herein the t_2^4 electronic configuration is viewed as the t_2^2 hole configuration and the excited-states ${}^3\mathrm{T}_1$ and ${}^1\mathrm{T}_2$ are obtained from the DFT single-determinant calculations as follows [12]:

$$E({}^3\mathrm{T}_1) = E(|\,\xi^+\eta^+\,|),$$
$$E({}^1\mathrm{T}_2) = 2[E(|\,\xi^+\eta^-\,|) - E(|\,\xi^+\eta^+\,|)] + E({}^3\mathrm{T}_1), \quad (3)$$

where ξ, η, and ζ are the components of t_2 orbitals. Thus the excited-states ${}^3\mathrm{T}_1$ and ${}^1\mathrm{T}_2$ can be obtained by $\xi^+\eta^+$ and $\xi^+\eta^-$ hole occupancy, which can be achieved by triplet and singlet setting, respectively. The excited-state ${}^5\mathrm{T}_2$ is obtained by the constrained occupancy approach with the $t_2^2e^2$ electronic configuration at the GGA+U framework. Besides, the geometry configuration of the non-Jahn-Teller ground state is obtained by optimizing the total energy of the constrained occupancy of three electrons occupying three t_2 orbitals and one electron being equally distributed over two e orbitals in octahedral coordination. Then the total energy of the ground state is calculated at such a geometric configuration with the DFT+U or HSE06 method. The detailed projected Mn^{3+}-d orbitals' density of states for both the ground and the various excited states can be found in Fig. S4 of the Supplemental Material [46].

The equilibrium geometric configurations of ground and excited states are obtained by geometric optimization with the corresponding electronic configuration. We note that in our calculations we ignore the small geometric relaxation of ${}^3\mathrm{T}_1$ and ${}^1\mathrm{T}_2$ as both are of the same t_2^4 electronic configuration. Based on the Franck-Condon principle, the excitation and emission energies are obtained by the ΔSCF method using the corresponding geometric structures [60,62].

The multiplet splitting is obtained by wave function based multiconfigurational calculations, as implemented in the MOLCAS package [63]. A defect cluster $[MnO_6]^{9-}$ with the Mn^{3+} ion at the center is constructed based on the DFT-optimized crystal structure. The *ab initio* model potential (AIMP) embedded cluster approach [64] is applied and the energy spectrum of Mn^{3+} is calculated at the state-average complete-active-space self-consistent-field (SA-CASSCF)/MS-CASPT2 [65–67] level. In the SA-CASSCF calculations, the following energy averages are minimized: The average of five states derived from the quintuplet states (${}^5\mathrm{E}$, ${}^5\mathrm{T}_2$), the average of five states derived from the triplet states (${}^3\mathrm{T}_1$, ${}^3\mathrm{E}$), and the average of five states derived from the singlet states (${}^1\mathrm{T}_2$, ${}^1\mathrm{E}$).

III. RESULTS AND DISCUSSION

A. Luminescent properties of Mn^{3+} in YAG

1. Formation energies of the native defect and Mn dopant

The garnet system crystallizes in the $Ia3d$ space group with the stoichiometric formula $A_3B_2B'_3O_{12}$ composed of interconnected $[AO_8]$ dodecahedra, $[BO_6]$ octahedra, and $[B'O_4]$ tetrahedra with D_2, C_{3i}, and S_4 point group symmetry, respectively. Each oxygen atom is a member of two dodecahedrons, one octahedron and one tetrahedron. In the case of YAG, the B and B' sites are all occupied by aluminum ions and manganese can substitute the dodecahedral Y ($Mn_{Y_{dod}}$), the octahedral Al ($Mn_{Al_{oct}}$), and the tetrahedral Al ($Mn_{Al_{tet}}$).

In order to evaluate the Mn site occupancy and valence states, the formation energies of Mn dopants and intrinsic defects have been calculated. The main intrinsic defects, cation and oxygen vacancies and antisite defects are taken into consideration [68]. To sustain the stable YAG phase, the chemical potentials are restricted by

$$\tfrac{3}{2}\Delta\mu_{Y_2O_3} + \tfrac{5}{2}\Delta\mu_{Al_2O_3} = \Delta H^f_{Y_3Al_5O_{12}}. \quad (4)$$

$\Delta H^f_{Y_3Al_5O_{12}}$ is the formation enthalpy of YAG with respect to Y_2O_3 and α-Al_2O_3 raw materials, where the latter are limited by $\Delta\mu_{Y_2O_3} \leqslant 0$ and $\Delta\mu_{Al_2O_3} \leqslant 0$. Here the equal contribution to formation enthalpy is first considered, where $\Delta H^f_{Y_3Al_5O_{12}} = -1.00$ eV, $\Delta\mu_{Y_2O_3} = -0.33$ eV and $\Delta\mu_{Al_2O_3} = -0.20$ eV. The chemical potential of oxygen can be related to partial pressure, p, and temperature, T, by [57]

$$\mu_O = \frac{1}{2}E_{O_2} + \Delta\mu_O, \quad (5a)$$

$$\Delta\mu_O = \frac{1}{2}k_BT\left[\ln\left(\frac{pV_Q}{kT}\right) - \ln Z_{rot} - \ln Z_{vib}\right]. \quad (5b)$$

Here V_Q is the quantum volume $(h^2/2\pi mk_BT)^{3/2}$ and Z_{rot} and Z_{vib} are the rotational and vibrational partition functions. Here k_B and h are the Boltzmann and Planck constants and m is the mass of the oxygen molecule. In experiments, the sintering temperature is above 1500 °C and an inert growth atmosphere is adopted to obtain the luminescence of manganese trivalent state [24]. Applying the experimental conditions $T =$ 1700 K and partial pressure $p = 0.01$ to Eq. (5b) leads to $\Delta\mu_O = -1.5$ eV. Then the chemical potential μ_O is obtained via Eq. (5a), with E_{O_2} being corrected by adding 1.36 eV per O_2, which is related to overbinding in the O_2 molecule by the usual GGA type functionals [69]. The formation energy of the overwhelmingly dominant manganese defect $Mn_{Al_{oct}}$, i.e., Mn^{3+} at the octahedral Al site, is determined with Eq. (2) from the manganese doping concentration per octahedral Al site of $c/N_{site} = 1.0$ at.% (i.e., 0.4 at.% of the total Al site from the original experimental work [24]) as $E^f \approx G^f = -k_BT\ln(c/N_{site})$, where the degeneracy factor has been omitted altogether with the formation entropy. Finally, the chemical potential of manganese μ_{Mn} is determined via Eq. (1) with the known E^f and those quantities on the right-hand side of Eq. (1) other than μ_{Mn}. The chemical potential μ_{Mn} should ensure that the MnO_2 and Mn_3O_4 phases are depleted. The formation energies of point defects calculated by GGA+U method are plotted in Fig. 1.

The charge neutrality condition leads to identical formation energies of the dominant positive charged defect $Mn^+_{Al_{oct}}$ (Mn^{4+}) and negative charged defect $Mn^-_{Y_{dod}}$ (Mn^{2+}) and the Fermi energy E_F^0 is estimated by the intersection of the two, as shown in Fig. 1. At this E_F^0, the formation energies of intrinsic defects are relatively much higher than those of the Mn dopant. Among the intrinsic defects, the antisite defect is dominant, which agrees with experiment [70–72] and it is known to act as a shallow electron trap and affect the structure, luminescence, and other properties of pure [73] and doped YAG [74]. The formation energies of manganese substitutions

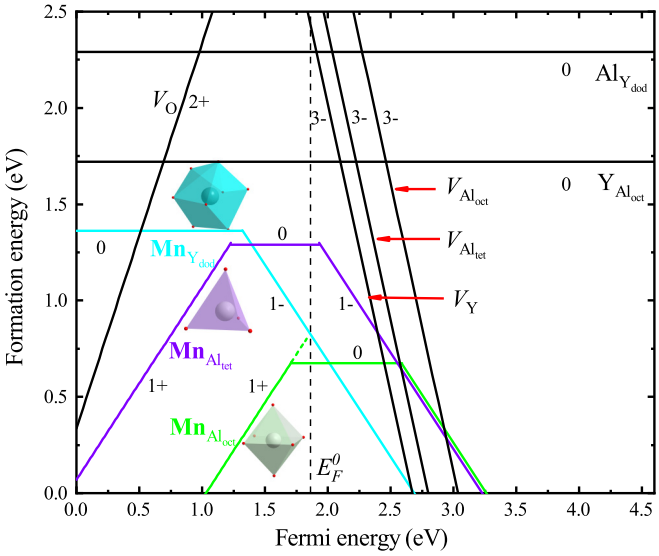

FIG. 1. The formation energies of Mn substitutions $Mn_{Y_{dod}}$, $Mn_{Al_{oct}}$, and $Mn_{Al_{tet}}$ and intrinsic defects as a function of Fermi energy. The energy of the VBM is set to zero and the equilibrium Fermi energy is labeled as E_F^0. The integer on a line segment indicates the total charge of the defect.

at the tetrahedral Al site are higher than at the octahedral Al site. Among all of the defects, $Mn^0_{Al_{oct}}$ (Mn^{3+}) is dominant in concentration, followed by $Mn^+_{Al_{oct}}$ (Mn^{4+}) and $Mn^-_{Y_{dod}}$ (Mn^{2+}).

The influence of chemical potentials on the formation energies of manganese in different valence states and site occupancy is now discussed. First, the relative chemical potentials of μ_Y and μ_{Al} are considered, which can be tuned by the formation enthalpy distribution on Y_2O_3 and Al_2O_3 within the two limits set by the depletion of Y_2O_3 or Al_2O_3 {see also Fig. S1(a) of the Supplemental Material [46]}. The lower μ_{Al} relative to μ_Y is beneficial for manganese to substitute the octahedral Al site with the Mn^{3+} valence state. By calculation, Mn^{3+} is dominant in all allowed chemical potential ranges, no matter for the Y_2O_3- or Al_2O_3-excess conditions. Furthermore, the oxygen chemical potential has no influence on the relative chemical potential of μ_Y and μ_{Al} and thus has little influence on manganese site occupancy and valence states.

2. *Geometric structure and luminescence of* Mn^{3+}

The Mn^{3+} ion is dominant in the octahedral Al^{3+} site among all of the defects with neutral charge, while the dominant positive and negative charged defects are $Mn^+_{Al_{oct}}$ (Mn^{4+}) and $Mn^-_{Y_{dod}}$ (Mn^{2+}), respectively. The concentrations of Mn^{2+} and Mn^{4+} are lower than that of Mn^{3+} and the luminescence energies of Mn^{2+} and Mn^{4+} are calculated in the Supplemental Material (Note 3) [46]. The $^4T_1 \rightarrow {}^6A_1$ emission energy of Mn^{2+} in dodecahedral ligands is calculated to be about 2.07 eV at the HSE06 level, which agrees well with the experimentally measured energy of 2.10 eV (~590 nm) in YAG [24].

We now study the luminescent properties of octahedral Mn^{3+} (d^4) in detail. The original [AlO_6] octahedron strictly follows C_{3i} symmetry but acts very close to O_h point group symmetry selection rules. The minor distortion from standard octahedral coordination is therefore neglected here. The five $3d$ orbitals split into the higher twofold degenerate e orbitals and the lower threefold degenerate t_2 orbitals in octahedral symmetry. The electronic configurations of the lowest-energy terms for the non-Jahn-Teller ground-state ^5E, the Jahn-Teller-split ground-state $^5E'$, and excited-states $^5T_2$, $^1T_2$, and $^3T_1$ are $t_2^3e^1$ (non-Jahn-Teller), $t_2^3e^1$ (Jahn-Teller-split), $t_2^2e^2$, t_2^4, and t_2^4, respectively. The energy levels can be obtained by the spin multiplicity control method supplemented by a constrained occupancy approach in the DFT framework and the equilibrium geometric configurations are obtained by geometric optimization with the corresponding electronic configuration, as described in the Methods section.

TABLE I. Mn–O bond lengths of [MnO_6] in the corresponding geometric configurations of $C(^5E)$, $C(^5E')$, $C(^5T_2)$, and $C(^3T_1)$ of Mn^{3+} in YAG host (in units of Å).

	$C(^5E)$	$C(^5E')$	$C(^5T_2)$	$C(^3T_1)$
Mn–O1(O4)	2.021	2.119	2.083	1.993
Mn–O2(O5)	2.020	1.969	2.046	1.976
Mn–O3(O6)	2.020	1.963	2.032	1.975
Average	2.020	2.017	2.054	1.981

First, the geometric configurations of the ground and excited states of Mn^{3+} are discussed. The equilibrium geometric configurations of the ^5E, $^5E'$, $^5T_2$, and $^3T_1$ states are labeled as $C(^5E)$, $C(^5E')$, $C(^5T_2)$, and $C(^3T_1)$. We ignore the small geometric relaxation of $^3T_1$ and $^1T_2$ because both are of the same t_2^4 electronic configuration. The six Mn–O bond lengths of octahedral [MnO_6] are listed in Table I. The six Mn–O bond lengths are equal in the non-Jahn-Teller $C(^5E)$ due to the half-filled t_2 subshell and the evenly filled e subshell. The Mn–O bond lengths of the original octahedral [AlO_6] are equal and measure 1.93 Å, which is smaller than for [MnO_6] due to the smaller ionic radius of Al^{3+}. The degenerate ground-state ^5E exhibits strong electron-lattice instability, which couples with the E_g-type mode (Q_ϑ and Q_ε), and yields an orbitally nondegenerate Jahn-Teller-split $^5E'$ and $^5E''$ states. The average Mn–O bond length of $C(^5E')$ is close to that of $C(^5E)$. However, $C(^5E')$ mainly shows a tetragonal compression displacement (Q_ϑ) relative to $C(^5E)$. Also, the average Mn–O bond length of $C(^5T_2)$ is larger than that of $C(^5E)$ since two electrons occupy the e subshell, while the average Mn–O bond length of $C(^3T_1)$ is smaller than that of $C(^5E)$ because the e orbitals are empty.

The detailed energy levels at the geometric configurations of $C(^5E)$, $C(^5E')$, $C(^5T_2)$, and $C(^3T_1)$ are shown in Fig. 2. The solid lines—calculated at the HSE06 level—give the lowest multiplet energy, whereas the dotted lines calculated by MOLCAS give the multiplet splittings. The splitting of $^5E''$ relative to $^5E'$ can also be estimated by the energy difference of the KS orbital at the HSE06 level (gray solid lines), which is close to the splitting obtained by MOLCAS (black dotted lines). It is noted that due to convergence problem in applying the constrained occupancy approach to the $t_2^2e^2$ electronic configuration in the HSE06 calculation, the $^5T_2$

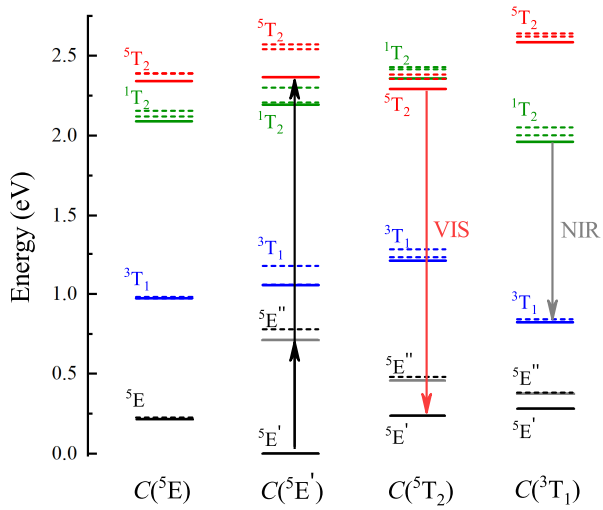

FIG. 2. The energy levels of Mn^{3+} calculated at the corresponding geometric configurations of $C(^5E)$, $C(^5E')$, $C(^5T_2)$, and $C(^3T_1)$. The solid lines are calculated at the HSE06 level and the dotted lines are the multiplet splittings, which are calculated by MOLCAS.

energy is not obtained directly but by adding the crystal-field splitting between the highest e and the highest t_2 KS orbitals to the energy of the ground-state $^5E'$ calculated at the same geometric configuration. The crystal-field splitting is obtained with the HSE06 calculation for the electronic configuration when the four electrons are spread equally onto the 5 spin up t_2 and e orbitals. Other calculation methods, GGA+U, SCAN+U [75,76], HSE06, and MOLCAS [63], are compared in Note 4 of the Supplemental Material [46].

At the non-Jahn-Teller $C(^5E)$ configuration, the multiplets are close to degenerate. The little distortion from standard octahedral coordination leads to small multiplet splitting. The calculated energy levels at the non-Jahn-Teller $C(^5E)$ geometric configuration are adopted to estimate the Racah parameter B as 857 cm^{-1} (see more details in Note 5 of the Supplemental Material [46]). The ligand field strength of Mn^{3+} is calculated to be 2.17 eV, which is obtained as the difference of average t_2 orbital and average e orbital energies in octahedral ligands at the HSE06 level, and the value is close to the $^5T_2$ energy level. Besides, the ligand field strength of Mn^{3+} in the YAG host is smaller than that in the $ZnGa_2O_4$ host [12], which leads to lower $^5T_2$ and higher $^1T_2$ excited states in the YAG host. Thus both red and NIR luminescence are observed in the YAG host [24], while only NIR luminescence is observed in the $ZnGa_2O_4$ host [77]. However at $C(^5E')$, the Jahn-Teller-split ground state is lower in energy and the excited states are all slightly higher relative to the energy levels at $C(^5E)$. By our calculation, the energies of the spin-allowed excitations $^5E' \rightarrow {}^5E''$ and $^5E' \rightarrow {}^5T_2$ are 0.71 and 2.37 eV, respectively. Experimentally, the infrared and visible excitation energies are correspondingly 0.82 and 2.43 eV in the Mn-doped YAG crystal [24]. Besides, the excited-state $^1T_2$ at $C(^3T_1)$ is lower in energy than the $^5T_2$ at $C(^5T_2)$ by 0.34 eV. The small geometric relaxation of $C(^3T_1)$ and $C(^1T_2)$ is ignored since both are of the same t_2^4 electronic configuration. The calculated emission energies of $^5T_2 \rightarrow {}^5E'$ and $^1T_2 \rightarrow {}^3T_1$ are 2.06 and 1.14 eV, respectively, which are coincident with the observed red and NIR emissions at 2.00 and 1.08 eV. The detailed excitation and emission energies are listed in Table II. To conclude, Mn^{3+} is excited vertically from the stable ground-state $^5E'$ to $^5T_2$, thermalizes quickly to the equilibrium geometric configuration $C(^5T_2)$, and then relaxes nonradiatively to the $^1T_2$ state at $C(^1T_2)$, which is slightly lower in energy than the $^5T_2$ at the $C(^5T_2)$ geometry. Thus at sufficiently low temperature, the population of the $^1T_2$ excited state is decisive, leading to the observation of NIR emission, $^1T_2 \rightarrow {}^3T_1$. However, at sufficiently high temperature, the population at the $^5T_2$ excited state increases and its large spin-allowed radiative transition rate leads to the observation of the (visible) red emission $^5T_2 \rightarrow {}^5E'$.

TABLE II. Experimental [24] and calculated excitation and emission energies of Mn^{3+} in YAG host (in units of eV).

Excitation	Calc.	Expt.	Emission	Calc.	Expt.
$^5E' \rightarrow {}^5E''$	0.71	0.89	$^5T_2 \rightarrow {}^5E'$	2.06	2.00
$^5E' \rightarrow {}^5T_2$	2.37	2.43	$^5T_2 \rightarrow {}^5E''$	1.84	1.64
			$^1T_2 \rightarrow {}^3T_1$	1.14	1.08
			$^1T_2 \rightarrow {}^5E'$	1.68	1.70
			$^1T_2 \rightarrow {}^5E''$	1.58	1.41

In Mn-doped YAG, the NIR and red emissions can both be observed at room temperature, but only NIR emission is observed at low temperature. It can be roughly deduced that for the comparable NIR and red emissions, the stable $^5T_2$ state should be higher than $^1T_2$ by 0.2 eV in energy, according that the radiative transition rate of $^5T_2 \rightarrow {}^5E'$ emission is about *500 times* larger than that of $^1T_2 \rightarrow {}^3T_1$ emission [24]. Here the energy difference of the stable $^5T_2$ state relative to $^1T_2$ is calculated to be about 0.34 eV, which is slightly higher and supports the observation of NIR and red emissions at room temperature in YAG crystal. Hence the experimental results are well reproduced except that the Jahn-Teller effect is systematically underestimated by about 0.2 eV. However, we note that the average bond length is smaller by about 0.5% and the Jahn-Teller distortion is larger by about 10% for the HSE06 relaxed geometric structures, which leads to a larger Jahn-Teller splitting ($^5E'$ and $^5E''$ splitting) of 0.81 eV.

3. *The APES of* Mn^{3+}

For a clearer understanding of the excitation, emission, and the electron-lattice interaction, the APESes have been calculated. The vibrations of the [MnO_6] octahedron are classified in terms of six moiety modes [78], which include three even-parity A_{1g}, E_g, and T_{2g} modes. The A_{1g} (Q_a) and E_g (Q_ϑ and Q_ε) modes are considered here for analyzing quenching processes [24,28]. The A_{1g} mode yields a systematic change in the metal ion-ligand distance. For the E_g modes, Q_ϑ and Q_ε are the components of E_g-type distortions of tetragonal and rhombic symmetry, respectively.

In octahedral coordination,

$$Q_a = \sqrt{6}(R_{ax} + R_{eq1} + R_{eq2})/3, \tag{6a}$$

$$Q_\vartheta = 2\sqrt{3}(R_{ax} - R_{eq})/3, \tag{6b}$$

$$Q_\varepsilon = R_{eq1} - R_{eq2}, \tag{6c}$$

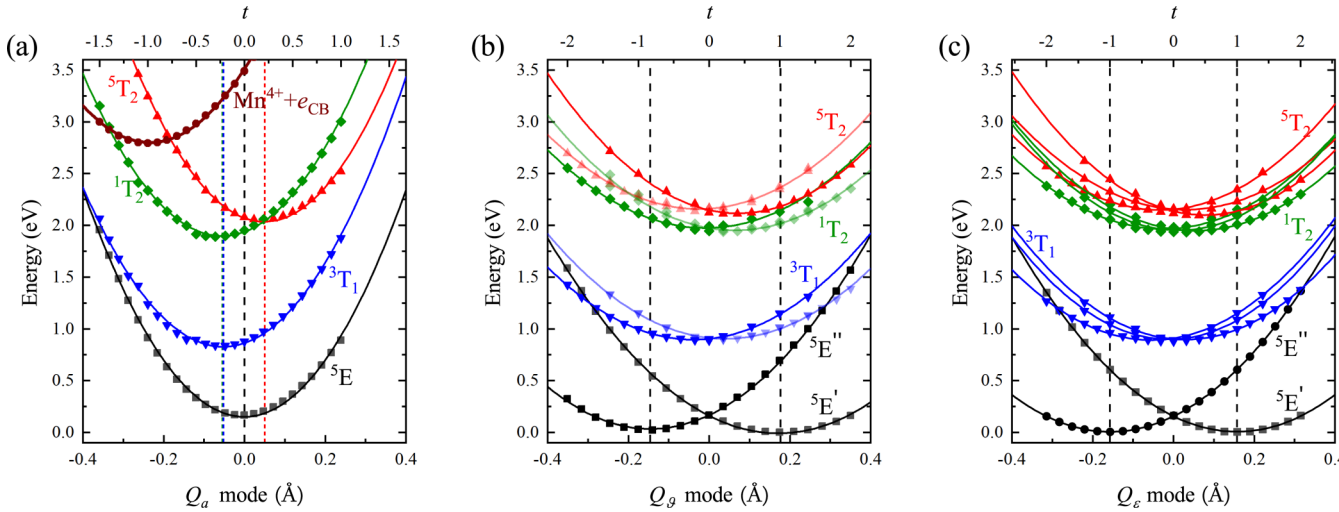

FIG. 3. The APESes along Q_a (a), Q_ϑ (b), and Q_ε (c) moiety modes. The top abscissa t is the mixing parameter used in obtaining intermediate structures from two reference ones. Parameter $t = 0$ corresponds to $C(^5\mathrm{E})$, and $t = -1$, 1, and 1 in (a)–(c) corresponds to $C(\mathrm{Mn}^{4+})$, $C(^5\mathrm{E}')_{Q_\vartheta}$, and $C(^5\mathrm{E}')_{Q_\varepsilon}$, respectively. The bottom abscissa is the corresponding magnitude of moiety modes. The points are calculated results and the lines are fitted in the harmonic approximation. In (b), light and dark colors are of single and double degeneracies, respectively.

where R_{ax}, R_{eq1}, and R_{eq2} are the change of axial and equatorial distances of [MnO_6] respective to non-Jahn-Teller $C(^5\mathrm{E})$ geometry [79]. The $C(\mathrm{Mn}^{4+})$ configuration mainly shows a systematic shrink ($Q_a < 0$) relative to $C(^5\mathrm{E})$. Then, we construct a series of interpolated structures which are obtained by $C(^5\mathrm{E}) + t[C(^5\mathrm{E}) - C(\mathrm{Mn}^{4+})]$. For each interpolated structure, the six bond lengths in the [MnO_6] moiety can be determined, and their changes relative to the non-Jahn-Teller structure are obtained, and such changes are characterized by Q_a determined in Eq. (6a) for the A_1 symmetry displacements of the six O ligands. The APESes of ground and various excited states along Q_a are plotted in Fig. 3(a). The $C(^5\mathrm{E}')_{Q_\vartheta}$ configuration mainly shows a tetragonal compression distortion (Q_ϑ) relative to $C(^5\mathrm{E})$. $C(^5\mathrm{E}')_{Q_\varepsilon}$ is obtained by geometric optimization with fixed Mn–O1 and Mn–O4 bonds, and the obtained Mn–O1(O4), Mn–O2(O5), and Mn–O3(O6) bond lengths are 2.02, 2.10, and 1.94 Å, respectively. The obtained $C(^5\mathrm{E}')_{Q_\varepsilon}$ configuration mainly shows a rhombic distortion (Q_ε) relative to $C(^5\mathrm{E})$. Similar to the APESes along Q_a, we construct two series of interpolated structures $C(^5\mathrm{E}) + t[C(^5\mathrm{E}')_{Q_\vartheta} - C(^5\mathrm{E})]$ and $C(^5\mathrm{E}) + t[C(^5\mathrm{E}')_{Q_\varepsilon} - C(^5\mathrm{E})]$, obtain Q_ϑ [Eq. (6b)] and Q_ε (Eq. (6c)), and plot their APESes in Figs. 3(b) and 3(c), respectively.

Thus the APESes at Q_a (a), Q_ϑ (b), and Q_ε (c) moiety modes are plotted in Fig. 3, where the top abscissa t is the mixing parameter used in obtaining intermediate structures from two reference ones and the bottom abscissa is the corresponding magnitude of moiety modes. All geometric structures are described relative to $C(^5\mathrm{E})$ and all energies are calculated relative to the lowest Jahn-Teller-split ground-state energy of $^5\mathrm{E}'$. The points in Fig. 3 are the calculated energy levels of the relevant electronic configuration at interpolated geometric configurations, where the lowest multiplets are calculated by the GGA+U method (for computational resources) and the multiplet splittings are calculated by MOLCAS. The lines are fitted in the harmonic framework as [24,80,81]

$$\varepsilon_i(Q) = \tfrac{1}{2}K_i(Q - Q_{i0})^2 + \varepsilon_{i0}, \tag{7}$$

where K_i is the force constant, Q_{i0} is the equilibrium coordinate, and ε_{i0} is the energetic minimum. The fitted force constants are close for different electronic configurations and the detailed fitting data are listed in Table S6 of the Supplemental Material [46].

As shown in Fig. 3(a), the equilibrium coordinate $Q_{a0} < 0$ for both $^3\mathrm{T}_1$ and $^1\mathrm{T}_2$ excited states, which indicates a slight shrinkage of bond length, whereas $Q_{a0} > 0$ for the $^5\mathrm{T}_2$ excited state, i.e., indicating a slight expansion. This is coincident with the obtained excited-state equilibrium geometric configuration, as shown in Table I. The activation energy at the Q_a mode is high and the energy difference of $^5\mathrm{T}_2$ and $^3\mathrm{T}_1$ is 1.08 eV at the HSE06 level, indicating a weak multiphonon nonradiative relaxation of $^5\mathrm{T}_2 \rightarrow {}^3\mathrm{T}_1$ via the Q_a distortion mode. Besides, the APES of the ionized excited-state $\mathrm{Mn}^{4+}+e_{\mathrm{CB}}$ is plotted, which shows a much larger shrinkage of bond length compared with the $^3\mathrm{T}_1$ and $^1\mathrm{T}_2$ excited states. Here the electron transfer from the $3d$ orbital of Mn^{3+} to the conduction band (CB) is denoted as the ionization transition $\mathrm{Mn}^{3+} \leftrightarrow \mathrm{Mn}^{4+}+e_{\mathrm{CB}}$. The excited-state $\mathrm{Mn}^{4+}+e_{\mathrm{CB}}$ is relatively higher in energy than the $^5\mathrm{T}_2$ excited state in the YAG:Mn system. Ionization quenching is not severe either, in agreement with experimental results [24].

Along the Q_ϑ moiety mode, Fig. 3(b), the Jahn-Teller-split lower states are labeled as $^5\mathrm{E}'$ or $^5\mathrm{E}''$ with tetragonal symmetry stretching or compression distortion, respectively. Both are onefold degenerate. The energetic minimum $\epsilon_{\vartheta 0}$ of $^5\mathrm{E}'$ is slightly lower in energy than that of $^5\mathrm{E}''$ by 0.025 eV and is lower in energy than that of the non-Jahn-Teller $^5\mathrm{E}$ state by 0.164 eV at the GGA+U level. However, the degenerate T states ($^5\mathrm{T}_2$, $^3\mathrm{T}_1$, and $^1\mathrm{T}_2$ excited states) can each split into a twofold degenerate E_g state and a onefold degenerate B_{2g} state with tetragonal symmetry distortion, which are labeled by light and dark colors, respectively, in Fig. 3(b). Besides, the equilibrium coordinates $Q_{\vartheta 0}$ of the $^5\mathrm{T}_2$, $^3\mathrm{T}_1$, and $^1\mathrm{T}_2$ excited states are much smaller than that of the $^5\mathrm{E}$ ground state along the Q_ϑ mode. However, at the Q_ε moiety mode with rhombic symmetry, Fig. 3(c), the degeneracy is fully lifted.

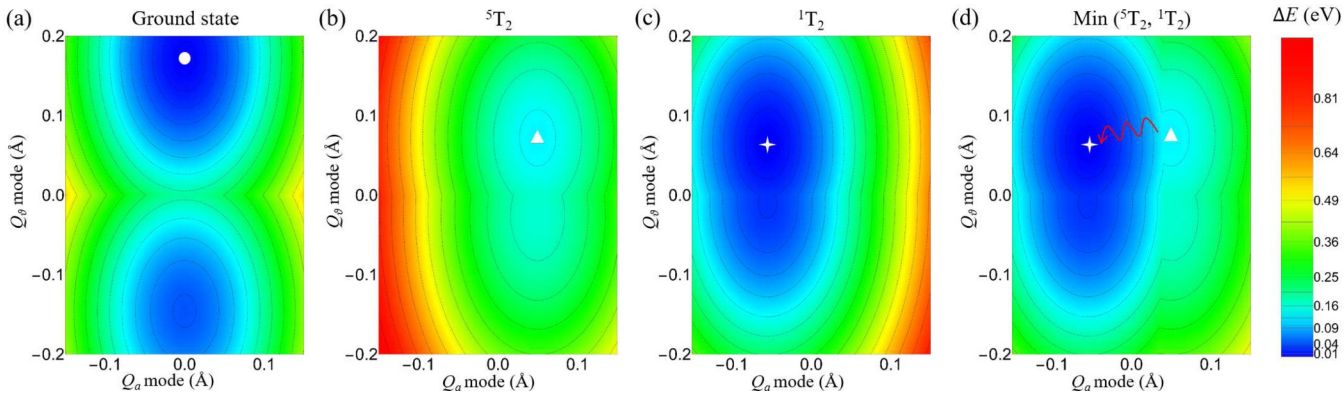

FIG. 4. The APESes of ground state (a), $^5T_2$ (b), $^1T_2$ (c), and min($^5T_2$, $^1T_2$) (d) at Q_a and Q_ϑ double moiety modes. It is noted that the energies in (b)–(d) are relative to the minimum energy of the $^1T_2$ state.

The intersections of $^5T_2$ and $^3T_1$ along Q_ε and Q_ϑ modes are also very high, indicating weak multiphonon nonradiative relaxation also via these two distortion modes [28].

The above discussions focus on APES along a single mode. Some discussions of the APES along two distortion modes are given in the following. Previously, electronic coupling with two modes of E_g type has been discussed [82] in the case of standard octahedral coordination. The "Mexican hat" APES is obtained for the ground-state ^5E interacting linearly with Q_ε and Q_ϑ modes (E_g type), which is approximately described by $\epsilon(\rho,\phi) = \frac{1}{2}K\rho^2 \pm \rho|F_E|$ to the second order. Here the distortion magnitude ρ_0 is about 0.16 Å and the Jahn-Teller stabilization energy is 0.17 eV at the GGA+U level. Three paraboloids interact at the reference configuration for the triplet terms interacting with Q_ε and Q_ϑ modes (E_g type). The high-order coupling terms lead to the ground states at $C(^5E')_{Q_\vartheta}$ smaller than the saddle point at $C(^5E')_{Q_\varepsilon}$ by ∼0.01 eV.

Then, the electron-lattice couplings with Q_a (A_{1g}) and Q_ϑ (one of the E_g modes) double moiety modes are calculated, as shown in Fig. 4. There are two wells along $Q_a = 0$, due to coupling with Q_ϑ, for the ground state in Fig. 4(a). One of these is the most stable ground-state $^5E'$ (marked with a white circle). When Mn^{3+} is excited vertically from the stable ground-state $^5E'$ to the excited-state $^5T_2$ at sufficiently low temperature, the excitation relaxes first to the most stable $^5T_2$ excited state marked with a triangle in Figs. 4(b) and 4(d), then the coupling with both Q_a and Q_ϑ leads to nonradiative relaxation from the $^5T_2$ APES across to the APES of the $^1T_2$ excited state shown in Figs. 4(c) and 4(d), and eventually to the population of the $^1T_2$ well [the white cross in Figs. 4(c) and 4(d)]. This leads to the occurrence of NIR emission $^1T_2 \rightarrow {}^3T_1$. However, at sufficiently high temperature, the $^5T_2$ well is populated as an endeavor to achieving thermal equilibrium population before decaying to the ground states. This leads to the red emission from $^5T_2$ at the expense of the $^1T_2$ emission.

B. Trends of optical transitions of Mn^{3+} doped in the garnet series

1. Effects of the ligand environment on the luminescence of Mn^{3+}

The phenomenological Tanabe-Sugano model can be employed to reveal the ligand-field strength dependence of Mn^{3+} energy levels. The energy of the $^5T_2$ excited state relative to the ^5E ground state is dominated by ligand field strength, and the $^5T_2$ energy level increases as the ligand field increases. The energy of the $^1T_2$ level decreases as the ligand field increases, and the energy of the $^1T_2$ excited state relative to $^3T_1$ is dominated by Coulomb repulsion and it is almost independent of ligand-field strength.

In our work, the variation trends of energy levels and photoluminescent properties of Mn^{3+} in a series of $A_3B_2B'_3O_{12}$ garnet hosts, YAG, YGG, GGG, and CGGG, have been studied systematically with first-principles calculations.

First, the ranges of allowed chemical potentials of composition elements are determined by various chemical constraints by following Refs. [83–85]. Then, the formation energies of Mn substitution and intrinsic defects are calculated and the ranges of chemical potentials for Mn^{3+} to be dominant are discussed (see more details in Note 2 of the Supplemental Material [46]). For YAG, YGG, and GGG hosts, the intrinsic defect concentrations are small compared with that of the Mn dopant, while in the CGGG host, the antisite defect concentrations are large and comparable with that of the Mn dopant. The lower chemical potential of B ion, μ_B, induces manganese substituted at octahedral B sites to form Mn^{3+}. By calculation, Mn_B^0 (Mn^{3+}) dominates in all the allowed chemical potential ranges in YAG, YGG, and GGG hosts, whereas the dominant manganese site occupancy and valence states in the CGGG host depend on the determined Fermi energy level, and Mn_{Ga}^0 (Mn^{3+}) is dominant over other Mn valences and substitutions over a broad range of chemical conditions.

The energy levels of octahedral Mn^{3+} have been calculated at the equilibrium geometric configurations of the non-Jahn-Teller ground-state $C(^5E)$, Jahn-Teller-split ground-state $C(^5E')$, and excited-states $C(^5T_2)$ and $C(^3T_1)$, as shown in Fig. 5. The calculated energy levels at the non-Jahn-Teller configuration $C(^5E)$ are adopted to estimate the Racah parameter B and the values are all around 860 cm^{-1} in a series of garnet hosts (see more details in Note 5 of the Supplemental Material [46]). The ligand field strengths are 2.17, 2.12, 2.07, and 1.99 eV, respectively, for the YAG, YGG, GGG, and CGGG hosts. These are obtained as the difference of the average t_2 orbital and average e orbital energies in octahedral coordination at the HSE06 level. Thus the ligand field strength of Mn^{3+} decreases for YAG > YGG > GGG > CGGG. The excitations of Mn^{3+} at the stable Jahn-Teller-split

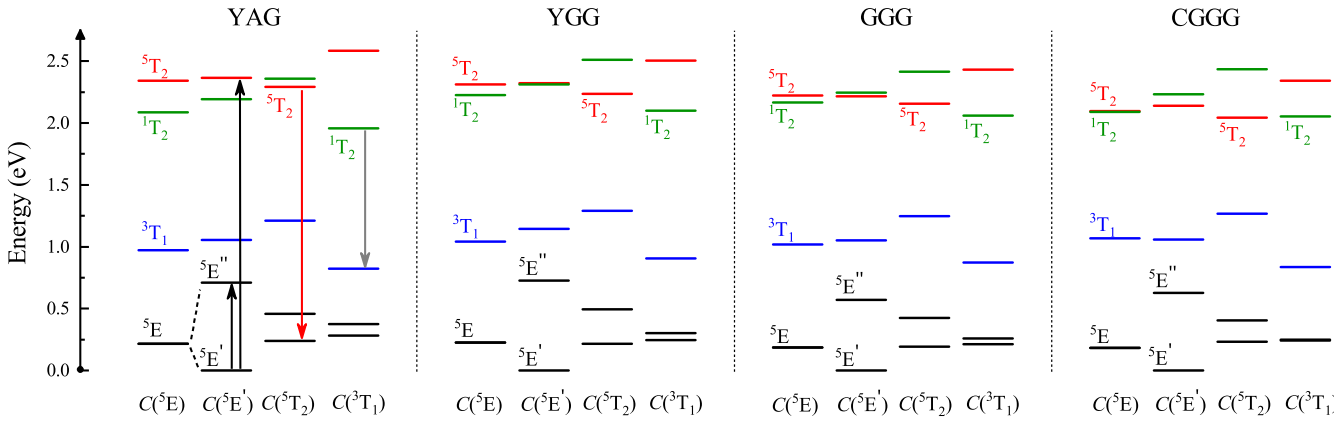

FIG. 5. The energy levels calculated at corresponding geometric configurations of $C(^5E)$, $C(^5E')$, $C(^5T_2)$, and $C(^3T_1)$ in YAG, YGG, GGG, and CGGG hosts.

ground-state $C(^5E')$ are the spin-allowed infrared $^5E' \rightarrow {}^5E''$ and visible $^5E' \rightarrow {}^5T_2$ transitions. By calculation, the visible $^5T_2 \rightarrow {}^5E'$ emission energies are 2.06, 2.02, 1.97, and 1.81 eV for the YAG, YGG, GGG, and CGGG hosts, respectively, which show redshift as the ligand field decreases. The NIR $^1T_2 \rightarrow {}^3T_1$ emission energies are calculated as 1.14, 1.19, 1.19, and 1.21 eV for the YAG, YGG, GGG and CGGG hosts, respectively, which show no significant dependence on the ligand field strength. Besides, the energies of the weak intensity emissions $^1T_2 \rightarrow {}^5E'/{}^5E''$ with $\Delta S = 2$ have been calculated and the dependence on the ligand field is opposite compared with $^5T_2 \rightarrow {}^5E'$. The detailed calculated excitation and emission energies are plotted in Fig. 6 for comparison with experimental results, and good overall agreement is achieved.

We now discuss the temperature dependence of the emissions. In room-temperature experiments [24], a NIR emission ~1150 nm is observed for YAG:Mn^{3+}. This emission is very weak for YGG:Mn^{3+} but not observed in the other crystals. Besides, a red emission is observed in all crystals at room temperature. However, a weak red emission is observed at low temperature for CGGG:Mn^{3+} only, while the NIR emission is present for all of the systems. The red emission corresponds to $^5T_2 \rightarrow {}^5E'$ and the NIR emission is the $^1T_2 \rightarrow {}^3T_1$ transition. The different behavior may be related to the relative energy of the $^5T_2$ and $^1T_2$ excited states. By calculation, the energy of the stable excited-state $^5T_2$ [$^5T_2$ level at $C(^5T_2)$] relative to that of the stable excited-state $^1T_2$ [$^1T_2$ level at $C(^1T_2)$] is largest in the YAG host and smallest in the CGGG host. The relative energies are correspondingly 0.34, 0.14, 0.10, and −0.01 eV in the YAG, YGG, GGG, and CGGG hosts. By considering the temperature-dependent population and the ratio of radiative relaxation rate between $^5T_2$ and $^1T_2$ excited states, the relative energy of $^5T_2$ with respect to $^1T_2$ should be ~0.2 eV for comparable NIR and red emissions at room temperature, as discussed above. Thus the NIR emission at room temperature is due to the large energy of $^5T_2$ relative to $^1T_2$, i.e., to the large ligand field strength. As mentioned above, the energies of $^5T_2$ relative to $^1T_2$ are 0.34 eV for YAG and 0.14 eV for YGG. The former is larger than 0.2 eV, while the latter is comparable with 0.2 eV, which leads to the occurrence of NIR emission in the YAG host and a very weak NIR emission in the YGG host at room temperature. Similarly considering the temperature-dependent population and the radiative relaxation rate of the $^5T_2$ and $^1T_2$ excited states, the relative energy of $^5T_2$ relative to $^1T_2$ should be ~0.003 eV for comparable red and NIR emissions at the low temperature of 5 K. The calculated relative energy of −0.01 eV for CGGG is compatible with experimental observations that $^5T_2$ emission still dominates at 5 K.

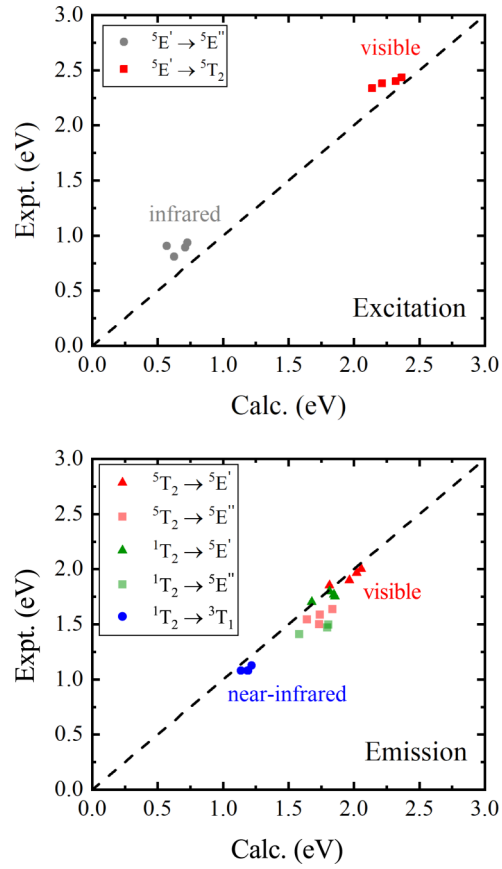

FIG. 6. Calculated versus experimentally reported [23,24] excitation and emission energies of Mn^{3+} in garnets. The dotted $y = x$ lines are plotted as a guide for the eyes.

The luminescence of Mn^{2+} and Mn^{4+} in garnet hosts is now briefly mentioned. By calculation, the emission energy of Mn^{2+} in dodecahedral oxygen coordination is calculated to be ~2.1 eV at the HSE06 level. Experimentally, a weak ~590 nm emission is observed in YAG:Mn. Thus it is attributed to Mn^{2+} in dodecahedral coordination and the formation energy of dodecahedral Mn^{2+} is lower in YAG than in the other crystals. Besides, the emission energy of Mn^{4+} in octahedral coordination is ~2.0 eV at the HSE06 level, which has been shown by a previous study to overestimate the emissions [12], and the observed ~650 nm emission arises from Mn^{4+} in octahedral coordination (see more details in Note 3 of the Supplemental Material [46]).

2. *Trends in the quenching process of* Mn^{3+}

The quenching of the red Mn^{3+} emission $^5T_2 \rightarrow {}^5E$ with temperature has been reported in the literature [24] and the quenching temperatures are in the order YAG $\gg$ YGG $>$ GGG $\gg$ CGGG. The calculated energy differences of $^5T_2$ and $^3T_1$ at $C(^5T_2)$ are correspondingly 1.08, 0.94, 0.91, and 0.78 eV for Mn-doped YAG, YGG, GGG, and CGGG crystals, which may enable nonradiative multiphonon luminescence quenching. When the energy difference increases, the nonradiative decay process involves a larger number of phonons and consequently its transition probability becomes smaller. Hence the critical temperature of the de-excitation transition increases with the larger ligand field strength. The required number of phonons is correspondingly 28, 28, 24, and 21 when the effective phonon energy $\hbar\omega = 306$ cm^{-1} is applied [24]. However, the energy difference in the YAG host is close to that in YGG and GGG hosts and it is somewhat contradictory to the experimental results [24], where the quenching temperature in YAG:Mn^{3+} is much higher than for other garnet hosts.

We notice that the ionized excited-state $Mn^{4+}+e^-_{CB}$ is comparable in energy with the $^5T_2$ excited state in garnets so that the quenching processes through ionization are possible at high temperature. The relative energies (i.e., stable $Mn^{4+}+e^-_{CB}$ relative to the stable $^5T_2$ excited state) are 1.29, 0.43, 0.43 and 0.70 eV for YAG, YGG, GGG and CGGG, respectively. The Mn^{4+}/Mn^{3+} transition energy levels relative to the CB minimum are plotted in Fig. S2. It should be noticed that the relative energy for CGGG is larger than that for YGG/GGG. However, there are large concentrations of Ga_{Ge} and Ge_{Ga} antisite defects, which can lower the CB and this leads to the much lower quenching temperature for CGGG. Besides, the luminescence quenching temperature for Mn^{3+} in $Y_3Sc_2Ga_3O_{12}$ (YSGG) and $Gd_3Sc_2Ga_3O_{12}$ (GSGG) is similar to that for CGGG [24]. There are a large number of antisite defects in YSGG/GSGG solid solutions, which leads to the low luminescence quenching temperature. Hence the appearance of luminescence of Mn^{3+} requires a low Mn^{4+}/Mn^{3+} transition energy relative to CB or band tail, and a potentially large band gap of host.

C. The effect of pressure on photoluminescence of Mn^{3+}

Due to the large radius of 3*d* orbitals and lack of shielding by outer filled shells, the electronic states of Mn^{3+} are sensitive to the local ligand environment, i.e., to the symmetry, bond lengths, angles, and coordination polyhedra. The effect of the ligand environment on the luminescent properties of Mn^{3+} may be revealed by pressure. The effects of high pressure on luminescence have been experimentally studied for CGGG:Mn^{3+} [23]. Figure 7 displays the calculated energies of $^5T_2 \rightarrow {}^5E'$, $^1T_2 \rightarrow {}^5E'$ and $^1T_2 \rightarrow {}^3T_1$ emissions as a function of pressure and average ground-state bond length. It is noted that the calculated pressure for the experimental structure under ambient conditions [42] is not zero in the DFT calculations due to error. Hence the pressure adopted in Fig. 7 is the change of calculated pressure. By applying pressure, the Jahn-Teller structural distortion effect on the ground state does not have a significant change, whereas the average bond length decreases with pressure. The dependence of average bond length on pressure is calculated to be about -4.29×10^{-4} Å/kbar.

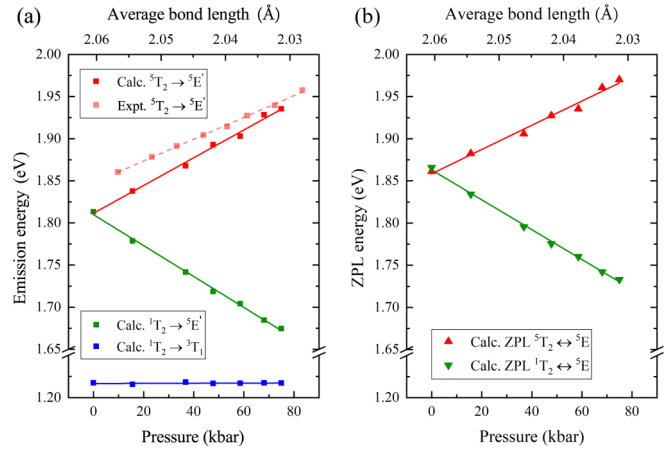

FIG. 7. The corresponding calculated emission energies (a) and ZPL energies (b) as a function of pressure and average bond length. The light red circles are experimental data [23] and the lines are linear fitting.

As shown in Fig. 7(a), the red emissions show a blueshift with pressure, and the dependence of the $^5T_2 \rightarrow {}^5E'/{}^5E''$ emission energy on pressure is calculated to be $1.65/1.67\times10^{-3}$ eV/kbar, which is slightly larger than experimental results of $1.29/1.31\times10^{-3}$ eV/kbar [23]. However, the $^1T_2 \rightarrow {}^5E'$ emissions exhibit a redshift with pressure. The dependence of $^1T_2 \rightarrow {}^5E'$ emission energy on pressure is calculated to be 1.77×10^{-3} eV/kbar. By contrast, the $^1T_2 \rightarrow {}^3T_1$ emission energy is 1.22 eV and is independent of pressure. Also, the ZPL energies of the $^5T_2$ and $^1T_2$ excited states relative to ^5E have calculated and their trends versus the pressure are plotted in Fig. 7(b). The two slopes are opposite but are of similar absolute values. The $^1T_2$ excited state can be much lower in energy than the $^5T_2$ excited state at high pressure, which enhances the NIR $^1T_2 \rightarrow {}^3T_1$ emission. Furthermore, our calculations show that the Mn^{4+}/Mn^{3+} transition level shifts upward due to the compression of ligands, which is beneficial for the stabilization of Mn^{4+} (rather than Mn^{3+}) at octahedral sites. Note that the photoluminescence of Mn^{4+} is observed experimentally at high pressure [23]. The calculated results agree with and further enrich the phenomenological Tanabe-Sugano model, where the $^5T_2$ and $^1T_2$ excited states, relative to ground-state ^5E, show the inverse

dependence with ligand field strength, and the energy of $^1T_2$ relative to $^3T_1$ is independent of pressure.

IV. CONCLUSIONS

We have performed first-principles calculations based on DFT to systematically study the stabilization and luminescent properties of Mn^{3+} in a series of $A_3B_2B'_3O_{12}$ garnet hosts. The formation energy shows the dominance Mn^{3+} at the octahedral B site for a large range of chemical potentials. The excited states, excitation and emission energies of this Mn^{3+} moeity have then been analyzed in detail. The calculated energy levels of Mn^{3+} show that the characteristic infrared absorption is the Jahn-Teller-split $^5E' \rightarrow {}^5E''$ transition and the visible absorption band is the spin-allowed $^5E' \rightarrow {}^5T_2$ transition. The characteristic red and NIR emissions are attributed to the $^5T_2 \rightarrow {}^5E'$ and $^1T_2 \rightarrow {}^3T_1$ transitions, respectively. The experimental excitation, emission energies, and temperature-dependent red to NIR emissions are well reproduced by our calculations for a series of garnets.

The ligand environment effects on the luminescence of Mn^{3+} have been studied in detail for a series of garnets. The ligand field strength for Mn^{3+} in garnets decreases along the series YAG, YGG, GGG, and CGGG. The energy of $^5T_2$ relative to $^1T_2$ increases as the ligand field strength increases, which leads to a slight increase of the $^5T_2 \rightarrow {}^5E'$ emission energy, but has less impact on the $^1T_2 \rightarrow {}^3T_1$ emission energy. The higher energy of $^5T_2$ relative to $^1T_2$ also leads to the smaller population of the $^5T_2$ excited state relative to that of the $^1T_2$ excited state as the ligand field strength increases. This explains the experimental results for the temperature-dependent emissions for a series of garnets, such as the room-temperature NIR luminescence in the YAG host and the low-temperature red luminescence in the CGGG host. To further investigate the effect of the ligand environment on the luminescent properties of Mn^{3+}, the effect of pressure has been studied in our calculations. The negative dependence of pressure on bond length has been obtained and the opposite ligand field strength dependencies of the $^5T_2$ and $^1T_2$ excited states have been rationalized. The calculated blueshift of the red emission and the dependence on pressure are close to experimental results.

Furthermore, the APESes of Mn^{3+} at the octahedral Al site along the $[MnO_6]$'s A_{1g} and E_g moiety modes have been calculated and the curves can be fitted well with parabolae over an energy range of 2 eV. The energy difference between $^5T_2$ and $^3T_1$ is about 1.0 eV. Together with the high activation energy, this indicates a low multiphonon nonradiative decay rate, so that the quenching due to ionization has also been studied. The closeness of the sum of Mn^{3+}/Mn^{4+} transition level and the energy of the relaxed excited state to the CB (or shallow impurity levels) provide an efficient ionization quenching process at sufficiently elevated temperatures.

In short, first-principles calculations can serve as an effective and predictive tool for exploring the structure distortion, optical transitions, quenching processes, effects of pressure, ligand environment, and Jahn-Teller distortions on the luminescence of the transition metal Mn^{3+}.

ACKNOWLEDGMENTS

The numerical calculations were performed on the supercomputing system at the Supercomputing Center of the University of Science and Technology of China. This work was financially supported by the National Key Research and Development Program of China (Grant No. 2018YFA0306600) and the National Natural Science Foundation of China (Grants No. 11974338, No. 61635012, and No. 11874275). C.-G.M. acknowledges financial support of the China–Poland Intergovernmental Science and Technology Cooperation Program (Grant No. 2020[15]/10).

[1] S. S. Hong, M. Gu, M. Verma, V. Harbola, B. Y. Wang, D. Lu, A. Vailionis, Y. Hikita, R. Pentcheva, J. M. Rondinelli *et al.*, Science **368**, 71 (2020).
[2] M. Fiebig, T. Lottermoser, D. Meier, and M. Trassin, Nat. Rev. Mater. **1**, 1 (2016).
[3] Y. Li, S. Qi, P. Li, and Z. Wang, RSC Adv. **7**, 38318 (2017).
[4] D. I. Khomskii and S. V. Streltsov, Chem. Rev. **121**, 2992 (2020).
[5] R. A. Maier, E. Cockayne, M. Donohue, G. Cibin, and I. Levin, Chem. Mater. **32**, 4651 (2020).
[6] R. A. Maier, K. F. Garrity, A. Ozarowski, M. P. Donohue, G. Cibin, and I. Levin, Acta Mater. **207**, 116688 (2021).
[7] S. Adachi, J. Lumin. **202**, 263 (2018).
[8] S. Adachi, J. Lumin. **197**, 119 (2018).
[9] B. Su, G. Zhou, J. Huang, E. Song, A. Nag, and Z. Xia, Laser Photonics Rev. **15**, 2000334 (2021).
[10] Q. Zhou, L. Dolgov, A. M. Srivastava, L. Zhou, Z. Wang, J. Shi, M. D. Dramićanin, M. G. Brik, and M. Wu, J. Mater. Chem. C **6**, 2652 (2018).
[11] D. Chen, Y. Zhou, and J. Zhong, RSC Adv. **6**, 86285 (2016).
[12] Q. Chen, L. Shang, H. Xu, C. Ma, and C.-K. Duan, J. Phys. Chem. C **125**, 21780 (2021).
[13] L. Marciniak and K. Trejgis, J. Mater. Chem. C **6**, 7092 (2018).
[14] L. Dong, L. Zhang, Y. Jia, Y. Xu, S. Yin, and H. You, Inorg. Chem. **59**, 15969 (2020).
[15] Y. Liu, X. Zhang, Z. Hao, X. Wang, and J. Zhang, Chem. Commun. **47**, 10677 (2011).
[16] J. Zhang, X. Hou, S. Wang, and Z. Ye, Chem. Eng. J. **411**, 128448 (2021).
[17] P. B. Allen and V. Perebeinos, Phys. Rev. B **60**, 10747 (1999).
[18] L. Ren, Y. Wang, M. Wang, S. Wang, Y. Zhao, C. Cazorla, C. Chen, T. Wu, and K. Jin, J. Phys. Chem. Lett. **11**, 2577 (2020).
[19] N. Rajamanickam, T. H. Chowdhury, S. Isogami, and A. Islam, J. Phys. Chem. C **125**, 20104 (2021).
[20] A. B. Souchkov, J. R. Simpson, M. Quijada, H. Ishibashi, N. Hur, J. S. Ahn, S.-W. Cheong, A. J. Millis, and H. D. Drew, Phys. Rev. Lett. **91**, 027203 (2003).
[21] M. Nakayama, Y. Furukawa, K. Maeda, T. Yoshimura, H. Uga, and N. Fujimura, Appl. Phys. Express **7**, 023002 (2014).

[22] M. Czaja, R. Lisiecki, A. Chrobak, R. Sitko, and Z. Mazurak, Phys. Chem. Miner. **45**, 475 (2018).

[23] Y. Wang, D. Włodarczyk, M. G. Brik, J. Barzowska, A. N. Shekhovtsov, K. N. Belikov, W. Paszkowicz, L. Li, X. Zhou, and A. Suchocki, J. Phys. Chem. C **125**, 5146 (2021).

[24] S. Kück, S. Hartung, S. Hurling, K. Petermann, and G. Huber, Phys. Rev. B **57**, 2203 (1998).

[25] M. A. Noginov, G. B. Loutts, and M. Warren, J. Opt. Soc. Am. B **16**, 475 (1999).

[26] T. S. Davis, J. P. Fackler, and M. J. Weeks, Inorg. Chem. **7**, 1994 (1968).

[27] M. Grinberg, A. Mandelis, K. Fjeldsted, and A. Othonos, Phys. Rev. B **48**, 5922 (1993).

[28] M. N. Sanz-Ortiz and F. Rodríguez, J. Chem. Phys. **131**, 124512 (2009).

[29] C. Freysoldt, B. Grabowski, T. Hickel, J. Neugebauer, G. Kresse, A. Janotti, and C. G. Van de Walle, Rev. Mod. Phys. **86**, 253 (2014).

[30] Y. Jia, S. Poncé, A. Miglio, M. Mikami, and X. Gonze, Adv. Opt. Mater. **5**, 1600997 (2017).

[31] B. Lou, J. Wen, J. Cai, Y.-Y. Yeung, M. Yin, and C.-K. Duan, Phys. Rev. B **103**, 075109 (2021).

[32] M.-H. Du, J. Mater. Chem. C **2**, 2475 (2014).

[33] N. C. George, K. A. Denault, and R. Seshadri, Annu. Rev. Mater. Res. **43**, 481 (2013).

[34] Y. Mei and W. Yang, J. Phys. Chem. Lett. **10**, 2538 (2019).

[35] G. Kresse and J. Hafner, Phys. Rev. B **47**, 558 (1993).

[36] G. Kresse and J. Hafner, Phys. Rev. B **49**, 14251 (1994).

[37] P. E. Blöchl, Phys. Rev. B **50**, 17953 (1994).

[38] J. P. Perdew, K. Burke, and M. Ernzerhof, Phys. Rev. Lett. **77**, 3865 (1996).

[39] Kh. S. Bagdasarov, N. B. Bolotina, V. I. Kalinin, V. F. Karyagin, B. V. Kuz'min, L. A. Muradyan, S. N. Ryadnov, E. M. Uyukin, T. S. Chernaya, E. A. Fedorov, V. S. Chudakov, and V. I. Simonov, Soviet Phys. Crystallogr. **36**, 398 (1991).

[40] A. Verma, N. Malhan, and A. K. Ganguli, Mater. Lett. **81**, 242 (2012).

[41] A. C. S. Hamilton, G. I. Lampronti, S. E. Rowley, and S. E. Dutton, J. Phys.: Condens. Matter **26**, 116001 (2014).

[42] C. Liu, Z. Xia, M. S. Molokeev, and Q. Liu, J. Am. Ceram. Soc. **98**, 1870 (2015).

[43] H. Raebiger, S. Lany, and A. Zunger, Phys. Rev. B **79**, 165202 (2009).

[44] J. Heyd, G. E. Scuseria, and M. Ernzerhof, J. Chem. Phys. **118**, 8207 (2003).

[45] J. Heyd, G. E. Scuseria, and M. Ernzerhof, J. Chem. Phys. **124**, 219906 (2006).

[46] See Supplemental Material at http://link.aps.org/supplemental/10.1103/PhysRevB.105.035158 for the details of the tests of U_{eff}, k-point meshes and HSE06 methods; charge corrections and formation energies; Mn^{2+} and Mn^{4+} in garnets; comparison of calculation methods; the Δ/B value and Racah parameter B, which includes Refs. [47–53].

[47] E. B. Linscott, D. J. Cole, M. C. Payne, and D. D. O'Regan, Phys. Rev. B **98**, 235157 (2018).

[48] Z. Liu, N. Zhao, M. Li, Q. Yin, Q. Wang, Z. Liu, D. Shen, Y. Huang, H. Lei, K. Liu *et al.*, Phys. Rev. B **104**, 115122 (2021).

[49] Y. Yekta, H. Hadipour, E. Şaşıoğlu, C. Friedrich, S. Jafari, S. Blügel, and I. Mertig, Phys. Rev. Materials **5**, 034001 (2021).

[50] M. Cococcioni and N. Marzari, Phys. Rev. Materials **3**, 033801 (2019).

[51] S. Yoon, S. Lee, S. Pang, M. Kim, and Y.-K. Kwon, Phys. Rev. B **104**, 035158 (2021).

[52] Z. Barandiarán and L. Seijo, Can. J. Chem. **70**, 409 (1992).

[53] S. Sugano, *Multiplets of Transition-Metal Ions in Crystals* (Academic Press, New York, 2012).

[54] T. R. Durrant, S. T. Murphy, M. B. Watkins, and A. L. Shluger, J. Chem. Phys. **149**, 024103 (2018).

[55] S. Lany and A. Zunger, Phys. Rev. B **78**, 235104 (2008).

[56] S. Lany and A. Zunger, Modell. Simul. Mater. Sci. Eng. **17**, 084002 (2009).

[57] C. G. Van de Walle and J. Neugebauer, J. Appl. Phys. **95**, 3851 (2004).

[58] W. Jing, M. Liu, J. Wen, L. Ning, M. Yin, and C.-K. Duan, Phys. Rev. B **104**, 165104 (2021).

[59] Z. Feng, B. Lou, M. Yin, Y.-y. Yeung, H.-T. Sun, and C.-K. Duan, Inorg. Chem. **60**, 4434 (2021).

[60] H. Shi, D. Han, S. Chen, and M.-H. Du, Phys. Rev. Materials **3**, 034604 (2019).

[61] Y. Jia, A. Miglio, S. Poncé, X. Gonze, and M. Mikami, Phys. Rev. B **93**, 155111 (2016).

[62] A. Alkauskas, B. B. Buckley, D. D. Awschalom, and C. G. Van de Walle, New J. Phys. **16**, 073026 (2014).

[63] G. Karlström, R. Lindh, P.-Å. Malmqvist, B. O. Roos, U. Ryde, V. Veryazov, P.-O. Widmark, M. Cossi, B. Schimmelpfennig, P. Neogrady *et al.*, Comput. Mater. Sci. **28**, 222 (2003).

[64] L. Seijo and Z. Barandiaran, *Computational Chemistry: Reviews of Current Trends* (Singapore, 1999), Vol. 4, p. 55.

[65] K. Andersson, P. A. Malmqvist, B. O. Roos, A. J. Sadlej, and K. Wolinski, J. Phys. Chem. **94**, 5483 (1990).

[66] B. O. Roos, P. R. Taylor, and P. E. M. Sigbahn, Chem. Phys. **48**, 157 (1980).

[67] G. Ghigo, B. O. Roos, and P.-Å. Malmqvist, Chem. Phys. Lett. **396**, 142 (2004).

[68] N. Shiran, A. Gektin, K. Hubenko, V. Nesterkina, P. Arhipov, S. Tkachenko, and O. Sidletskiy, Functional Materials **23**, 191 (2016).

[69] L. Wang, T. Maxisch, and G. Ceder, Phys. Rev. B **73**, 195107 (2006).

[70] J. Dong and K. Lu, Phys. Rev. B **43**, 8808 (1991).

[71] F. A. Selim, D. Solodovnikov, M. H. Weber, and K. G. Lynn, Appl. Phys. Lett. **91**, 104105 (2007).

[72] A. B. Muñoz-García, E. Artacho, and L. Seijo, Phys. Rev. B **80**, 014105 (2009).

[73] V. Babin, K. Blazek, A. Krasnikov, K. Nejezchleb, M. Nikl, T. Savikhina, and S. Zazubovich, Phys. Status Solidi C **2**, 97 (2005).

[74] Y. Zorenko, A. Voloshinovskii, V. Savchyn, T. Voznyak, M. Nikl, K. Nejezchleb, V. Mikhailin, V. Kolobanov, and D. Spassky, Phys. Status Solidi B **244**, 2180 (2007).

[75] J. Sun, A. Ruzsinszky, and J. P. Perdew, Phys. Rev. Lett. **115**, 036402 (2015).

[76] G. S. Gautam and E. A. Carter, Phys. Rev. Materials **2**, 095401 (2018).

[77] Y.-P. Wang, H.-S. Zhang, L.-T. Lin, S.-F. Zhou, Y. Yao, X.-B. Yang, and Y.-J. Zhao, J. Appl. Phys. **125**, 095701 (2019).

[78] L. Ning, P. A. Tanner, and X. Shangda, Vib. Spectrosc. **31**, 51 (2003).

[79] F. Rodriguez and F. Aguado, J. Chem. Phys. **118**, 10867 (2003).

[80] N. M. Avram, M. G. Brik, C. N. Avram, I. Sildos, and A. M. Reisz, Solid State Commun. **149**, 2070 (2009).
[81] I. B. Bersuker, Chem. Rev. **101**, 1067 (2001).
[82] I. Bersuker, *The Jahn-Teller Effect* (Cambridge: Cambridge University Press, 2006).
[83] K. Simalaotao, P. Reunchan, N. Umezawa, J. T-Thienprasert, and A. Boonchun, J. Appl. Phys. **125**, 165703 (2019).
[84] P. Reunchan, N. Umezawa, S. Ouyang, and J. Ye, Phys. Chem. Chem. Phys. **14**, 1876 (2012).
[85] L. Bjaalie, A. Janotti, K. Krishnaswamy, and C. G. Van de Walle, Phys. Rev. B **93**, 115316 (2016).